Time Evolution of Entanglement of Electrons and Nuclei and Partial Traces in Ultrafast Photochemistry

Martin Blavier,[1,2] R. D. Levine,[2,3] F. Remacle[1,2]*

[1]Theoretical Physical Chemistry, University of Liège, 4000 Liège, Belgium

[2]The Fritz Haber Research Center for Molecular Dynamics, The Hebrew University of Jerusalem, 91904 Jerusalem, Israel

[3] Department of Chemistry and Biochemistry and Department of Molecular and Medical Pharmacology, David Geffen School of Medicine, University of California, Los Angeles, CA 90095, USA

Broad in energy optical pulses induce ultrafast molecular dynamics where nuclear degrees of freedom are entangled with electronic ones. We discuss a matrix representation of wave functions of such entangled systems. Singular Value Decomposition, (SVD) of this matrix provides a representation as a sum of separable terms. Their weights can be arranged in decreasing order. The representation provided by the SVD is equivalent to a Schmidt decomposition. If there is only one term or if one term is already a good approximation, the system is not entangled. The SVD also provides either an exact or a few term approximation for the partial traces. A simple example, the dynamics of LiH upon ultrafast excitation to several non-adiabatically coupled electronic states is provided. The major contribution to the entanglement is created during the exit from the Franck Condon region. An additional contribution is the entanglement due to the nuclear motion induced non-adiabatic transitions.

* Corresponding author, fremacle@uliege.be

1. Introduction

Progress in laser atto science has now reached the point where few cycle, few femtosecond pulses are available in the deep UV[1, 2] and could promote neutral polyatomic molecules to bound excited states, thereby providing new insights on photodynamics in small and bio molecules[3-9] and large band gap materials.[10] The broad energy width of 2-3 fs pulses in the deep UV means that several electronic states are coherently excited.[11, 12] The short excitation time also implies that the nuclear configuration of the molecules is localized in the Franck Condon (FC) region. Due to the localization the vibrational wave functions are coherent superpositions of stationary vibrational states. Even starting with a cold molecular ground state, shortly after excitation by the short pulse, the wave function of the excited state typically cannot be written as a product of electronic and vibrational wave functions. Rather, the wave function describes an entangled motion of electronic and nuclear modes meaning that they cannot be described independently of one another. There is no electronic state of the molecule nor is there a vibrational state.

Entanglement is an extensively discussed strictly quantum phenomena. [13-15] It is often, as in quantum computing,[14] used for (two or more) identical systems that are coupled. The early example was two entangled photons emitted from the same source.[16, 17] But the two systems need not be identical, one can entangle vibrational modes in a polyatomic molecule,[18] or scattering channels in chemical reactions.[19, 20] Entanglement between the electronic and nuclear degrees of freedom was previously studied for stationary eigenstates of vibronic Hamiltonians[21, 22] and also for time-dependent vibronic wave functions[23-26] Here we highlight the coupling of two motions that are characterized by qualitatively different time scales, the electrons and the nuclei and how it affects the time evolution of their entanglement. The entanglement of the two is the physical opposite of the Born-Oppenheimer separation. It is made possible by the ultrafast optical excitation.[27-29] Ultrafast attosecond photoionization and the resulting entanglement between the photoelectron and a cation can also be used to probe the vibrational coherences of the cation.[30]

To solve the dynamics it is practical to represent the Hamiltonian and other operators as matrices in a finite basis. For the electrons we use N_e adiabatic electronic states covering the energy span of the optical pulse. Since the initially excited state is in the FC region we use orthonormal functions $\left| g_i \right\rangle$ localized on points of a discrete grid, one grid per vibrational

coordinate.[11] For the LiH diatomic molecule that will be our numerical example we use a grid of N_g points. A wave function in a N_g x N_e dimensional space is a tensor product or explicitly a double sum of electronic and grid terms. The adiabatic electronic states, $\left| e_j \right\rangle$, are obtained by diagonalizing the electronic Hamiltonian at each grid point. Near points of avoided crossings such electronic states can be quite different for nearby grid points. The non crossing rule insures however that the index j is unique and therefore the wave function

$$\left| \Psi \right\rangle = \sum_{j=1}^{N_e} \sum_{i=1}^{N_g} a_{ij} \left| g_i \right\rangle \left| e_j \right\rangle \tag{1}$$

is a sum of terms separable in the electronic and vibrational (= grid) indices.

Our aim is to reduce the number of terms in Eq. (1) that are necessary for an exact or a realistic approximation. We shall show that a finite *single* sum of N_e or even fewer terms suffices. This resulting single sum of terms is equivalent to the Schmidt decomposition.[13, 14, 31] The number of terms in that single sum is called the Schmidt number or the rank of the state. It provides a quantification of the entanglement of the state: a separable state will have a Schmidt decomposition involving only one term and will therefore have a Schmidt number of 1 whereas an entangled state will have a larger Schmidt number. The compaction of the wave function to a single sum also offers a useful route to the partial traces. These arise when one intends to compute expectation values involving observables that act only on one system and not on the other.[14]

2. Theory

2.1 The matrix representation of the wave function

We rewrite the vector **a** of the coefficients of the wave function at each time point as a rectangular N_g x N_e matrix:

$$\mathbf{A} = \begin{pmatrix} a_{11} & a_{12} & \cdots & a_{1N_e} \\ a_{21} & a_{22} & \cdots & a_{2N_e} \\ \vdots & \vdots & \vdots & \vdots \\ a_{N_g 1} & a_{N_g 2} & \cdots & a_{N_g N_e} \end{pmatrix} \tag{2}$$

This operation is the inverse to the vectorization of a matrix[32] and is called matricization. It takes a clear advantage of the physics of the problem where each column is the coefficients along the grid of a particular electronic state while each row is the coefficients of the different electronic states at a particular grid point. The rectangular matrix $\mathbf{A}$ can be resolved using the singular value decomposition theorem,[33] SVD, in the form:

$$\mathbf{A} = \sum_n \sigma_n \mathbf{u}_n \mathbf{v}_n^\dagger \tag{3}$$

For the typical case where $N_g > N_e$, one can show that $\mathbf{A}$ has at most N_e finite singular values that are all positive and Σ is a diagonal matrix of dimension $N_e \times N_e$ with the singular values along its diagonal. $\mathbf{u}_n$ and $\mathbf{v}_n$ are respectively the left and right singular vectors of $\mathbf{A}$. The vectors can be chosen as orthonormal so that $\mathbf{A}\mathbf{v}_n = \sigma_n \mathbf{u}_n$ and $\mathbf{A}^\dagger \mathbf{u}_n = \sigma_n \mathbf{v}_n$. A compact form of the matrix $\mathbf{A}$ is $\mathbf{A} = \mathbf{U}\Sigma\mathbf{V}^\dagger$ and it is also useful to note the pair of compact identities $\mathbf{A}^\dagger \mathbf{A} = \mathbf{V}\Sigma^2\mathbf{V}^\dagger$ and $\mathbf{A}\mathbf{A}^\dagger = \mathbf{U}\Sigma^2\mathbf{U}^\dagger$.

2.2 The chemical physics of the singular vectors

The singular vectors are the eigenvectors of the square and non-negative matrices $\mathbf{A}^\dagger \mathbf{A}$ and $\mathbf{A}\mathbf{A}^\dagger$, explicitly $\mathbf{A}\mathbf{A}^\dagger \mathbf{u}_n = \sigma_n^2 \mathbf{u}_n$ and $\mathbf{A}^\dagger \mathbf{A}\mathbf{v}_n = \sigma_n^2 \mathbf{v}_n$. It follows that the singular vector $\mathbf{v}_n$ has the (shorter) length, N_e, and its components are the components of the different electronic states of the system in this n'th singular vector. We call the vectors $\mathbf{v}_n$ the electronic singular vectors below. On the other hand, the singular vector $\mathbf{u}_n$ has the (longer) length, N_g, and its components are the components of the different states of the grid in this singular vector. We call them the nuclear singular vectors. In the single sum of separable terms $\mathbf{v}_n$ is the electronic part and $\mathbf{u}_n$ is the nuclear or grid part.

The essential practical point is that the SVD theorem states that when we keep N_e terms, the maximal possible number, the SVD representation of $\mathbf{A}$ is exact. However, if we rank the

(positive) singular values σ_n by their decreasing size and keep only a smaller number, say, N_{min}, of terms in the sum

$$\mathbf{A} = \sum_{n=1}^{N\min} \sigma_n \mathbf{u}_n \mathbf{v}_n^\dagger \tag{4}$$

the approximation is the best possible one, in the sense of matrix norm, keeping only a smaller number, N_{min}, of terms in the sum. Keeping more terms by increasing the value of N_{min} provides a better (or unchanged) approximation. Note that the previous terms are unchanged and only one or more additional terms are added. The lowest number, $N_{min} = 1$, corresponds to the separable state, a state of Schmidt rank unity.

2.3 The partial traces

When one wants to consider observables defined only for a particular subsystem it is useful to define the concept of a partial trace. The expectation value of an observable $\hat{O}$ that is diagonal in the electronic subspace, $\left\{\left|e_j\right\rangle\right\}$, and independent of the nuclear system in the entangled state $\left|\Psi\right\rangle$, Eq. (1), is

$$
\begin{aligned}
\left\langle\Psi\middle|\hat{O}\middle|\Psi\right\rangle &= \sum_{j,i} \left\langle e_j,g_i\middle|\Psi\right\rangle\hat{O}\left\langle\Psi\middle|e_j,g_i\right\rangle \\
&= \sum_{j,i} \left\langle e_j\middle|\hat{O}\middle|e_j\right\rangle\left\langle e_j,g_i\middle|\Psi\right\rangle\left\langle\Psi\middle|e_j,g_i\right\rangle \\
&= \sum_j \left\langle e_j\middle|\hat{O}\middle|e_j\right\rangle\sum_i\left|a_{ij}\right|^2
\end{aligned}
\tag{5}
$$

This motivates the definition of a partial trace over the nuclear states as the density matrix

$$\bar{\rho}_{el} = \mathrm{Tr}_n\left(\left|\Psi\right\rangle\left\langle\Psi\right|\right) = \sum_{j,j'} \left|e_j\right\rangle\sum_i a_{ij}a_{ij'}^*\left\langle e_{j'}\right| \tag{6}$$

It is seen that the diagonal elements of the sum, $\sum_i \left|a_{ij}\right|^2$, are the populations of the different electronic states while the off-diagonal elements are the electronic coherences. This justifies regarding $\bar{\rho}_{el}$ as a density matrix for the electronic degrees of freedom. In terms of the matrix $\mathbf{A}$ on which we perform the SVD, we write the density $\bar{\rho}_{el}$ as

$$\bar{\rho}_{el} = \mathbf{A}^{\dagger}\mathbf{A} \tag{7}$$

Correspondingly one can define a partial trace over the electronic degrees of freedom:

$$\bar{\rho}_n = \mathrm{Tr}_{el}\left(|\Psi\rangle\langle\Psi|\right) = \Sigma_{i,i'}|g_i\rangle\left(\Sigma_j a_{ij}a_{i'j}^*\right)\langle g_{i'}| \tag{8}$$

with the matrix form $\bar{\rho}_n = \mathbf{A}\mathbf{A}^{\dagger}$. Note that both partial trace matrices have a unit trace as expected. Either one can be expressed in terms of the singular vectors, for example:

$$\bar{\rho}_{el} = \mathbf{A}^{\dagger}\mathbf{A} = \Sigma_n \sigma_n^2 \mathbf{v}_n \mathbf{v}_n^{\dagger} \quad , \quad \bar{\rho}_n = \mathbf{A}\mathbf{A}^{\dagger} = \Sigma_n \sigma_n^2 \mathbf{u}_n \mathbf{u}_n^{\dagger} \tag{9}$$

2.4 An optimal approximation

The Schmidt decomposition of the wave function keeping all the singular values is an exact representation. There is however an important secondary conclusion: The analysis based on the SVD theorem shows that the Schmidt decomposition of the wave function provides the minimal number of separable terms that are needed to achieve a given accuracy. The more terms are kept the more accurate is the result. Even keeping just one term, which is a separable approximation, is in general a better approximation than keeping just one term in the starting form, Eq. (1), of the wave function.

The Schmidt decomposition of the wave function is based on using Eq. (3) for the coefficients a_{ij} in Eq. (1)

$$
\begin{aligned}
|\Psi\rangle &= \sum_{j=1}^{N_e}\sum_{i=1}^{N_g}\left(\sum_{n=1}^{N}\sigma_n u_{in}v_{jn}^{\dagger}\right)|g_i\rangle|e_j\rangle \\
&= \sum_{n=1}^{N}\sigma_n\left(\sum_{i=1}^{N_g}u_{in}|g_i\rangle\right)\left(\sum_{j=1}^{N_e}v_{jn}^{\dagger}|e_j\rangle\right) \\
&= \sum_{n=1}^{N}\sigma_n|\mathbf{u}_n\rangle|\mathbf{v}_n^{\dagger}\rangle
\end{aligned}
\tag{10}
$$

Here N is the number of singular values or the Schmidt rank. If N is the number of singular values of the matrix $\mathbf{A}$, equations (2) and (3), then equation (10) is exact. When we rank the (non negative) singular values by size and keep the leading $N = N_{\min}$ values then equation (10) is the best separable approximation. As is clear from the derivation, the separable states are linear combinations of the basis states with weights determined by the singular vectors:

$$\left| \mathbf{u}_n \right\rangle = \sum_{i=1}^{N_g} u_{in} \left| g_i \right\rangle \ , \ \left| \mathbf{v}_n^\dagger \right\rangle = \sum_{j=1}^{N_e} v_{jn}^\dagger \left| e_j \right\rangle \tag{11}$$

As a practical matter note that when we increase the number N of terms in Eq. (10) we do not need to change the already included separable terms. The new terms add up without modification of the earlier ones.

From the expression of the wave function in terms of the singular components (Eq. (10)), one can readily write the expression of the full density matrix:

$$\rho(t) = \left| \Psi(t) \right\rangle \left\langle \Psi(t) \right| = \sum_{m,n}^{N_e} \sigma_m(t) \sigma_n(t) \left| \mathbf{u}_n \right\rangle \left| \mathbf{v}_n^\dagger \right\rangle \left\langle \mathbf{u}_m^\dagger \right| \left\langle \mathbf{v}_m \right|$$
$$= \sum_{m,n}^{N_e} \sigma_m(t) \sigma_n(t) \rho_{mn}(t) \tag{12}$$

Eq. (12) does not lead to a separable expression in terms of the partial traces $\bar{\rho}_{el}$ and $\bar{\rho}_{nucl}$ defined above. Its terms $\rho_{mn}(t)$ off diagonal in the singular index are essential for describing the vibronic coherences in observables such as the dipole moment or the total momentum, see the Results and Discussion section below.

2.5 An illustration of this approach: the photoexcitation of LiH

We chose the LiH molecule to provide an illustration for the description of the time evolution of the entanglement for two reasons: being a diatomic molecule, a grid-based description of the wavefunction is greatly simplified, thereby significantly decreasing the computational cost of the dynamics; and the computational data was already available within our group. The simple one-dimensional grid also allows developing a better intuition of the singular vectors of the nuclei as previously described.

The electronic structure of the LiH molecule was computed at the state averaged CAS-SCF (4, 20) level using the 6-311++G(3df, 3dp) Gaussian basis set as a function of the internuclear distance, as described in ref. [34]. Only the first seven Σ electronic states were retained in the description of the dynamics. This provided the potential energy curves (PEC) for each electronic state as well as the non-adiabatic couplings (NAC) between them. The potential energy curves, the NAC curves are plotted in Figure 1a. The curves of the

transition dipole curves are given in Figures S1 and S2 of the Electronic Supplementary Information (ESI).

The wavefunction of the molecular system is described onto a grid of 512 points along the internuclear distance R. In this basis, the wavefunction has the expansion given in Eq. (1).

In this basis, the matrix of the molecular Hamiltonian for the LiH molecule takes the following form (we use atomic units, a.u., throughout)

$$\mathbf{H}_{ij,kl}(t) = \mathbf{V}_{ij,kl}\delta_{ik}\delta_{jl} + \left(\mathbf{T_N}\right)_{ij,kl}\delta_{jl} - \left(\tau_{jl}\delta_{ik}\right)\cdot\mathbf{p}_{ij,kl} - \mathbf{E}(t)\cdot\left(\mu_{jl}\right)\delta_{ik} \qquad (13)$$

In Eq. (13), i and k are indices on the grid and j and l indices of the electronic states. $\mathbf{V}_{ij,kl}\delta_{ik}\delta_{jl}$ is diagonal on both nuclear (i,k) and electronic (j,l) indices and correspond to the potential energy for a given electronic state and at a given nuclear geometry. $\left(\mathbf{T_N}\right)_{ij,kl}\delta_{jl}$ is diagonal on electronic indices, but non-diagonal on the grid and describes the nuclear kinetic energy. This nonlocal operator is approximated by fourth order finite differences.[11] The third term describes the non-adiabatic interactions, which couple the derivative couplings between electronic states $\left(\tau_{jl}\delta_{ik}\right)$ and the momentum on the grid $\mathbf{p}_{ij,kl}$. The last term describes the interaction of the molecule with the electric field of the optical pulse, $\mathbf{E}(t)$, in the dipole approximation. The transition dipole moments between two electronic states, $\left(\mu_{jl}\right)\delta_{ik}$, are diagonal on the grid.

The quantum dynamics is computed by solving numerically the time-dependent Schrödinger equation using a fourth order Runge-Kutta method. The propagation in time of the coefficients, a_{ij}, is by the Hamiltonian using matrix-vector multiplication as was early on formulated by Dirac, $i\,da_{ij}(t)/dt = \sum_{kl} \mathbf{H}_{ij,kl}a_{kl}(t)$. The exciting pulse is given by Eq. (14) below. It is centered at 12.1 fs, its carrier frequency, $\hbar\nu$, is 5.5 eV, the amplitude of the electric field is 0.02 a.u. and its full width at half maximum (FWHM) is 1.98 fs. These parameters correspond to a deep UV optical pulse similar to those which could become readily available to experimentalists in the near future.[2]

$$E(t) = -\frac{d\mathbf{A}(t)}{dt} = |E_0|\, \hat{e} \exp\left(-\frac{(t-t_0)^2}{2\sigma^2}\right)\left(\cos(\omega t + \phi) - \frac{\sin(\omega t + \phi)(t-t_0)}{\omega \sigma^2}\right) \quad (14)$$

3. Results and discussion

To investigate the time evolution of the entanglement in the LiH molecule, we first computed the time evolution for the probabilities of each electronic state, j, $P_j(t) = \sum_i |a_{ij}(t)|^2$. This evolution is plotted in Figure 1b.
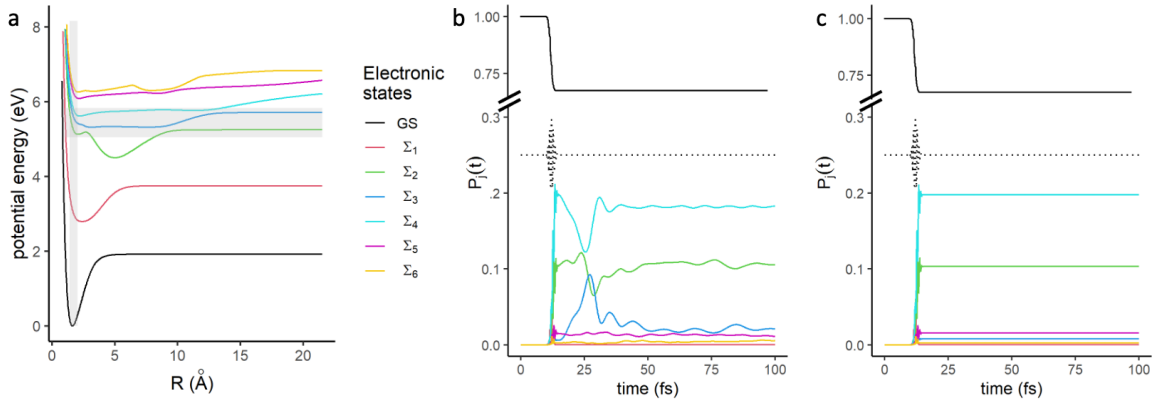

Figure 1. (a) Potential energy curves of the 8 lowest Σ states of LiH.[34] The FC region is shown the energy bandwidth of the UV pulse are shown in shaded grey areas. (b) Time evolution of the populations of the electronic states, $P_j(t) = \sum_i |a_{ij}(t)|^2$, computed for the dynamics that includes the NAC in the Hamiltonian (Eq. (13)) and (c) the dynamics without NAC (c). The excited electronic states are identified in the inset. The time profile of the electric field of the exciting pulse is represented by the black dotted line.

Before the pulse, the wave packet is localized only on the ground state (GS). The optical pulse then causes amplitude transfer from the GS towards excited electronic states which possesses the largest electric dipole moment from the GS in the FC region. These states are the Σ_4 and Σ_2 electronic states while Σ_3 is almost dark, see Figure S2 for the transition dipole moments. After the pulse, the population on the ground state remains essentially constant, whereas the populations of the higher excited electronic states significantly change in the first 50 fs due to the effect of non-adiabatic couplings (NAC). The strongest NACs

9

(Figure S1) are taking place between the pairs of states, Σ_2 - Σ_3, and Σ_3 - Σ_4, in the range of 2 to 5 Å, which results into an amplitude transfer from the two most populated excited states, Σ_2 and Σ_4, to Σ_3 at the exit of the FC region up to ≈ 25 fs and then to a transfer back to these two states from Σ_3 at ≈ 30 fs. At longer times, the populations in Σ_2 and Σ_4 are the largest and do not vary significantly. There are exchange of population between Σ_2 and Σ_3 due a smaller NAC coupling between 5 and 10 Å.

To gain insight into the impact of NAC in the entanglement during the time evolution, another dynamics was computed without including the NAC (which amounts to removing the $\left(\tau_{jl} \delta_{ik} \right) \cdot \mathbf{p}_{ij,kl}$ terms in the Hamiltonian of Eq. (13)). For comparison, the time evolution for the populations of each electronic state of this dynamics without NAC is shown in Figure 1c. They are stationary after the pulse. This does not mean, however, that the wave packets are not moving on their respective electronic state but rather that there is no amplitude transfer. Note also that when the NAC is not included in the dynamics, there is essentially no population in Σ_3.

We compute the SVD of the wave function at each time of the dynamical evolution to assess the rank of the best possible approximation of the wave function at each moment of the dynamics. At each value of time, we obtain a set of singular values, and a left and right eigenvector, the nuclear and electronic singular vectors respectively. The time evolution of the singular values, σ_n in Eq. (4), is plotted in Figure 2 for the case of the dynamics that includes the NAC in the Hamiltonian (Eq. (13)) shown in Figure 1b.
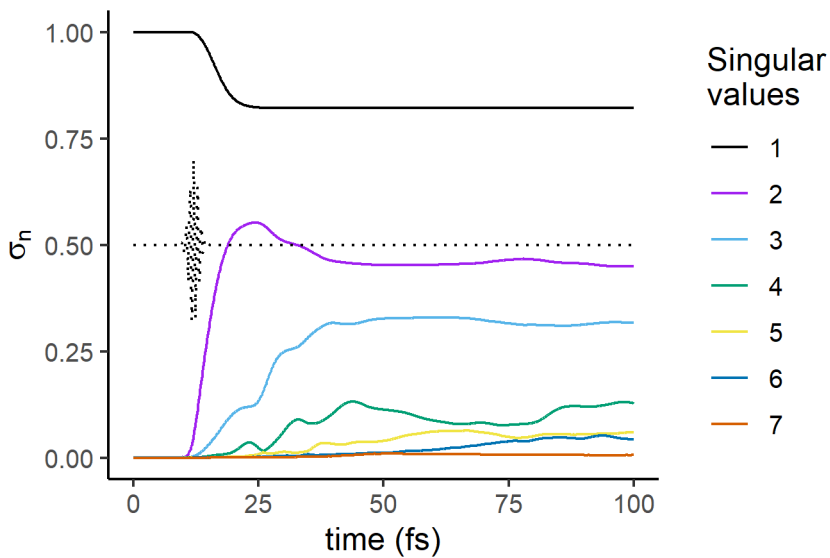
Figure 2. Time evolution of the singular values, σ_n, Eq. (4), computed for the dynamics that includes the NAC term in the Hamiltonian (Eq. (13)) shown in Figure 1b. The time profile of the electric field of the exciting pulse is shown in dotted lines.

Before the pulse, the wave packet is localized in the GS, a situation which is a trivial example of a separable state. This is confirmed by the presence of only one singular value (black line in Figure 2) in the decomposition. During the pulse, amplitude transfers begin to take place between the GS and the excited electronic states, leading to the appearance of second singular value (violet) in the second half of the pulse. The overall state of the molecule is now entangled, as its Schmidt decomposition (Eq. (10)) requires more than one term. Shortly after the end of the pulse, after ≈ 15 fs, a third singular value (blue) arises. A fourth and a fifth smaller singular values arise at later times, at 20 and 30 fs respectively and a 6th one at ≈ 60 fs. The 4th and 5th singular eigenvalues get very close at ≈ 25 fs and then at ≈ 70 fs, see figures S3 for a focus on this range of time. At each time step, the singular values are obtained as the eigenvalues of a semi-positive Hermitian matrix, Eqs. (9). When considered as a function of time, the different eigenvalues do not cross. The 4th and 5th singular eigenvalues get very close at ≈ 25 fs and then at ≈ 70 fs but do not cross since we have one dimension for the nuclear motion, see figures S3 for a focus on this range of time.

The first avoided crossing is due to the strong non adiabatic interaction between Σ_3 and Σ_2 in the range 3-5 Å (see Figure S1) and the second to the NAC between these two states at $\approx$ 10 Å. At the avoided crossings, the relative weights of the singular electronic eigenstates on Σ_3 and Σ_2 interchange (Figure 5c below and Figure S3) but there is no discontinuity in the singular nuclear states.

The significance of a singular value can be assessed from how much it contributes to the trace of the full density matrix, $\mathrm{Tr}\left[\rho(t)\right]=\sum_n \sigma_n^2(t)=1$. We show in Figure 3 the convergence of $\mathrm{Tr}\left[\rho(t)\right]$ computed for an increasing number of singular values. The trace of the density matrix is reaching values very close to unity with 2 singular values at the end of the pulse and a third and a fourth one are needed after ≈ 30 and ≈ 50 fs respectively. The 5th and the 6th have negligible contributions.
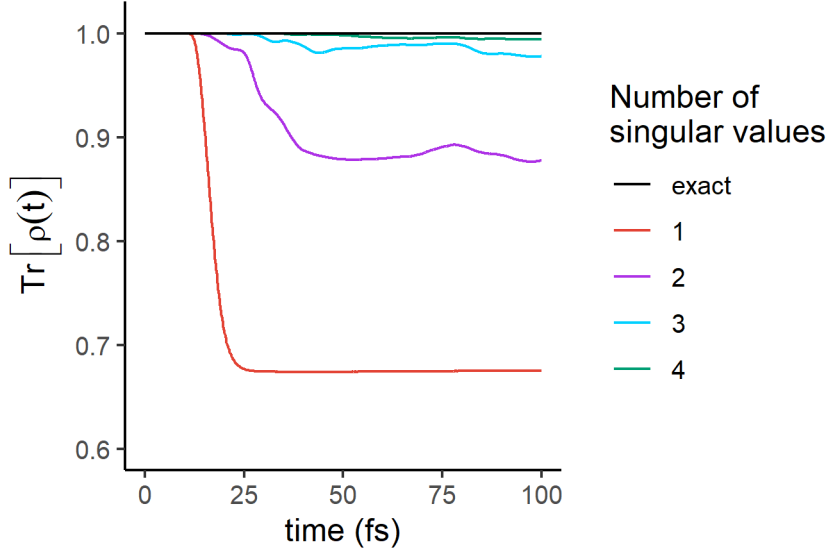
Figure 3. Convergence of $\mathrm{Tr}\left[\rho(t)\right]$ as a function of the number of singular values included in the sum. Red: only the largest singular value is included, violet: the first two are included, azure: the first three, green : the first four. At 100fs, about 2/3 of $\mathrm{Tr}\left[\rho(t)\right]$ is recovered by 1 singular value, 87% by 2, 95 % by 3 and 98 % by 4.

The time evolution of the entanglement of the wave function is governed by the time evolution of singular values shown in figure 2. In order to understand which features of the dynamics govern their timings, we next turn to the physical meaning of the left and right singular vectors in the decomposition (4).

As discussed in section 2 above, the right singular vectors, $\mathbf{v}_n$, represent the electronic component of a given term in the singular decomposition, Eq. (4). Their time evolution reflects the time evolution of the localization of the wave packet on the electronic states. The left eigenvectors, $\mathbf{u}_n$, correspond to the weights of the singular states on the grid and provide the complementary picture of their localization in the nuclear subspace as time evolves. In the following, we call the left singular eigenvectors, $\mathbf{u}_n$, and the right singular eigenvector, $\mathbf{v}_n$, the nuclear and electronic singular eigenvectors respectively.

The physical meaning of the first singular state in the singular decomposition (Eq. (4)) is seen in Figure 4a and b, where the weights of the electronic singular eigenvector, $\mathbf{v}_1$, on the electronic states are shown in panel a and the localization of the nuclear singular eigenvector $\mathbf{u}_1$ on the grid in panel b.
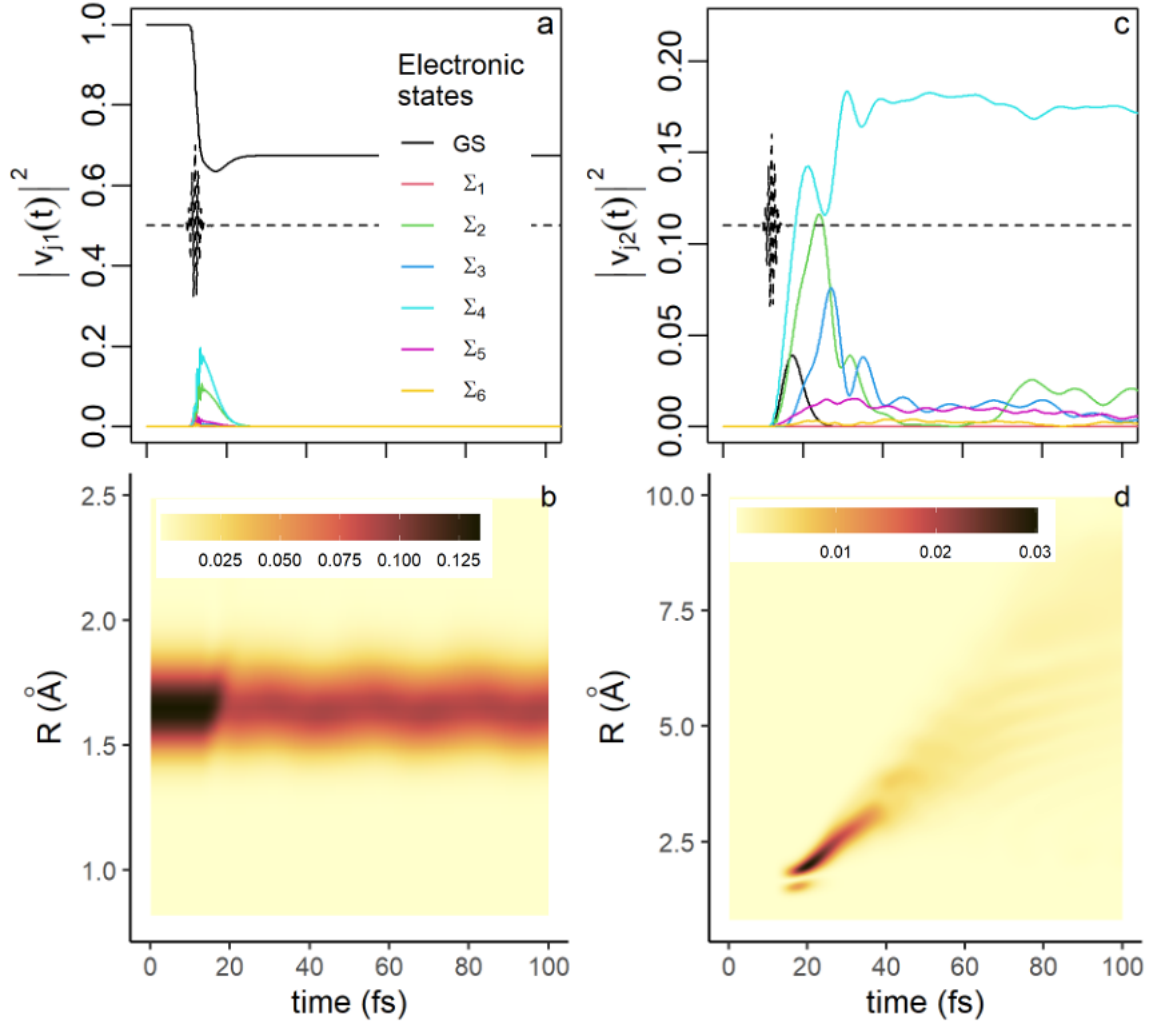
Figure 4. Physical meaning of the first and the second singular states. (a) Time evolution of the weights, $\left|v_{j1}(t)\right|^2$, Eq. (11), of the electronic singular eigenvector, $\mathbf{v}_1$, of the decomposition Eq. (4) on the electronic states for the first 100 fs of the dynamics (the color code is the same as in Figure 1, see inset). (b) Heatmap of the weights, $\left|u_{i1}(t)\right|^2$, Eq. (11), of the nuclear singular eigenvector, $\mathbf{u}_1$, on the grid points, i (R, ordinate) as a function of time (abscissa). (c) Time evolution of $\left|v_{j2}(t)\right|^2$, (d) Heatmap of localization of $\left|u_{i2}(t)\right|^2$ as a function of time on the grid. The weights are multiplied by square of the singular values, σ_n^2, n=1 or 2. The color code for the heatmaps is shown as an inset in b) and d).

As can be seen from Figures 4a and b, the first component of the singular decomposition, Eq. (4), is localized on the GS in the FC region. During and shortly after the pulse, $\mathbf{v}_1$

acquires significant weights on the Σ_2 and Σ_4 states (Fig. 4a). These are the states that fall in the energy bandwidth of the pulse (Figure 1a) and carry significant transition dipoles (Figure S2). Since the transfer of amplitude to excited states occurs in the FC region, the localization on the grid of these three electronic states is fully accounted for by the $\mathbf{u}_1$ nuclear singular vector during the pulse (figure 4b). After the pulse, the first component remains fully localized on the GS and in the FC region. Its magnitude decreases because only $\approx 70\%$ of the wave packet remains in the GS. Since the fraction of the wave packet localized on the GS is no longer an eigenstate, the oscillations seen in Figure 4b reflect the vibrational motion in the GS well.

The rise of the singular value of the second component, σ_2, in the second half of the pulse (see Figure 2) corresponds to the decrease in σ_1 when the wave packets on Σ_2 and Σ_4 begin exiting the FC region. At short time (up to 20 fs), the electronic singular vector, $\mathbf{v}_2$, (Figure 4c), is localized on Σ_4 and Σ_2, the two excited states most populated by the pulse (see Figure 1) and on the GS, with a rising smaller component on Σ_3. These four electronic states are still mainly localized in the FC region, as shown in Figure 4d. After 30 fs, $\mathbf{v}_2$ is localized on the Σ_4 state, which is the excited state with the highest population (Figure 1b). The changes in the electronic composition are reflected by the localization of nuclear singular vector, $\mathbf{u}_2$, on the grid shown in Figure 4d. The weight in the FC region progressively fades and the localization of the $\mathbf{u}_2$ vector shifts to larger R values, that reflects the motion of the wave packet to larger R values on the PEC shown in Figure 1a.
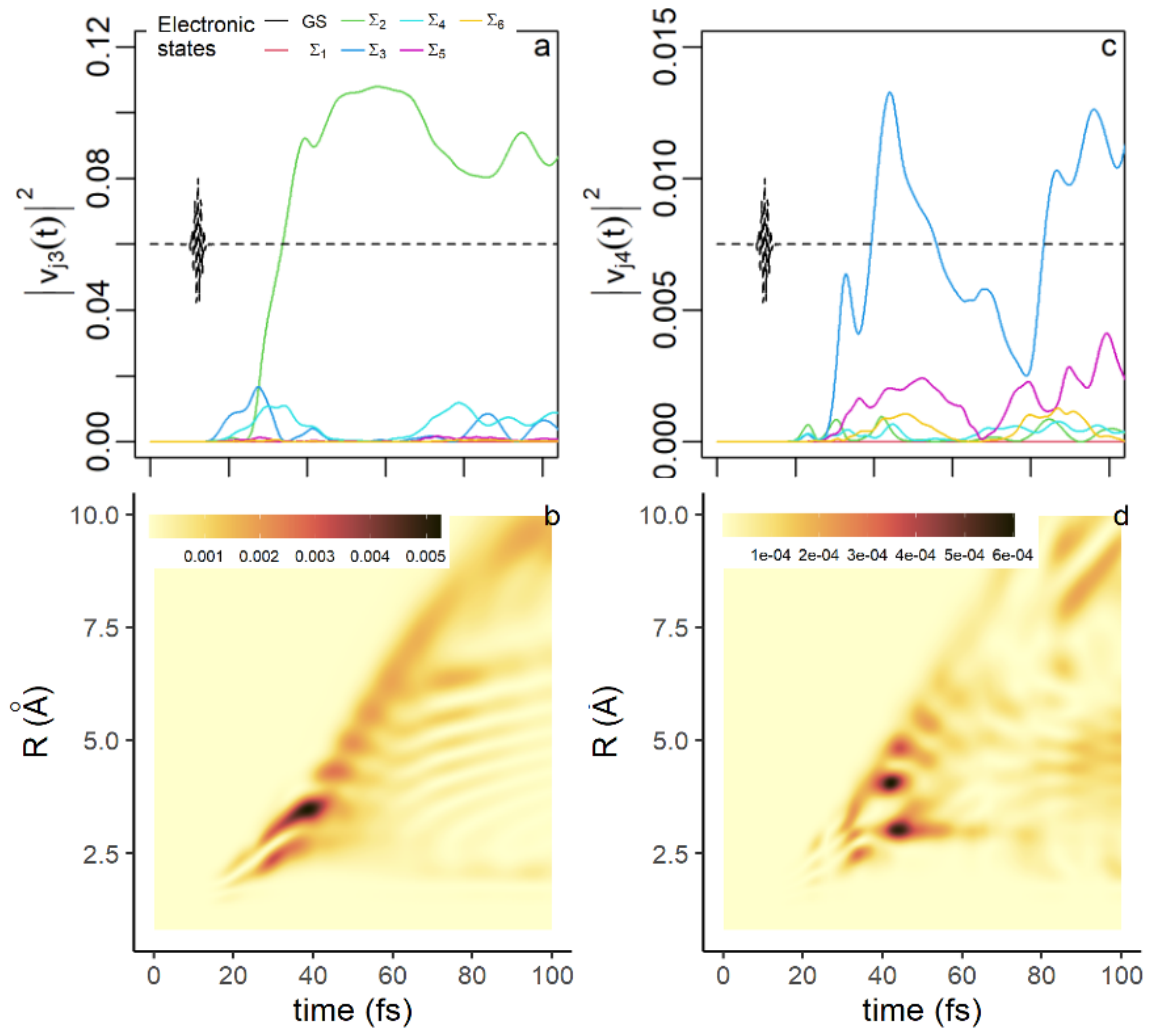
Figure 5. Physical meaning of the third and the fourth singular states. (a) The weights, $\left|v_{j3}(t)\right|^2$, Eq. (11), of the electronic singular eigenvector, $\mathbf{v}_3$, of the decomposition Eq. (4) on the electronic states (same color code as in figure 4). (b) Heatmap of the weights, $\left|u_{i3}(t)\right|^2$, Eq. (11), of the nuclear singular eigenvector, $\mathbf{u}_3$, on the grid points. (c) time evolution of the weights, $\left|v_{j4}(t)\right|^2$, of the fourth electronic singular eigenvector. (d) Heatmap of the localization of the weights, $\left|u_{i4}(t)\right|^2$, of the fourth nuclear singular eigenvector on the grid. The weights are multiplied by σ_n^2, $n = 3$ or 4.

The localization of the third component in electronic and grid subspaces is shown in Figures 5a and b respectively. This component becomes significant after 20 fs. Up to 25 fs, the

electronic singular vector, $\mathbf{v}_3$, is mostly localized on the Σ_3 state, whose population rises at the end of the pulse (see Figure 1b) due to the NAC at the exit of the FC region (see Figure S2). At 25 fs, the largest weight shifts from Σ_3 to Σ_2 to mainly localize on Σ_2 at long times. This shift coincides with the rise of the Σ_3 component in the fourth electronic singular vector $\mathbf{v}_4$ (figure 5c). The localization of the nuclear singular vector $\mathbf{u}_3$ on the grid (Figure 5b) reflects the shift in the dominant electronic state in $\mathbf{v}_3$. After 40 fs, one sees two branches for $\mathbf{u}_3$ on the grid, that reflect the double well of the PES of the Σ_2 state (Figure 1a). The main branch reflects the localization of the third component in the shallow well of Σ_2 at large R values while the less intense one corresponds to the fraction of the third component localized in the small well of Σ_2 close to the FC region. The fourth component (figure 5 c and d) has a more minor contribution to the dynamics due to the smaller value of $\sigma_4^2(t)$. After 25 fs, it localizes on the Σ_3 state with small weights on Σ_5 and Σ_6. At short time, the nodal patterns seen in Figure 5 b and d are mainly induced by the orthogonality of the $\mathbf{u}_n$ vectors. At longer time, in regions of the grid where the non adiabatic coupling is strong and two adiabatic states contribute to the electronic singular vector, these patterns are modulated by the beatings of the vibronic coherence in space and in time.

The increase of the number of singular values in the decomposition thus reflects the motion of the wave packets on the populated electronic states and more specifically its exit from the FC region. The motion of several wave packets on the grid leads to a change in the entanglement of the system. The switch of the electronic weights of Σ_2 and Σ_3 that occurs at ≈ 25 fs in the third SVD component results from the interplay between the changes in the gradients of the PES (Figure 1a) that drive the motion of the wave packets at different rates along the R coordinate and the localization of the Σ_2-Σ_3 NAC on the grid (figure S1).

We therefore compared the time evolution of the squares of the singular values, σ_n, for the dynamics with NAC with the time evolution for the dynamic without NAC shown in Figure 1c. They are shown in figure 6. This provides understanding on the origin of the rise of the third and fourth singular values.
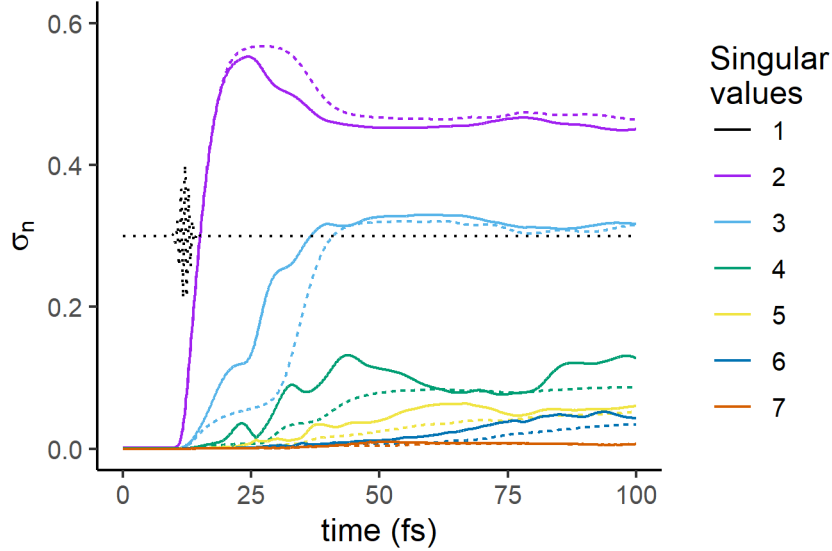
Figure 6. Time evolution of the singular values, σ_n, $n = 2$ to 7. Full line: computed for the dynamics with NAC (also shown in figure 2), dashed line: computed for the dynamics without NAC. The first singular value, σ_1 is not shown as there is essentially no difference in its value for the two computations.

Interestingly, as can be seen in Figure 6, the rise of σ_3 is also observed in the case of dynamics without NAC, but the onset of this increase occurs leads to a plateau at a small value, followed by a significant rise to a second plateau in the range 30-40 fs. The first plateau is not present in the dynamics with NAC for which σ_3 rises faster. This suggests that the NAC contributes significantly to the entanglement of the state of the molecule between 15 and 25 fs, after which the effect of the difference in the gradient of the PEC plays a significant role, as can be inferred from figures 1a and S1. In the dynamics without NAC, the onset of σ_3 is due to the gradient difference between the potential curves of the Σ_4 and the Σ_2 PEC in the range of R values between 2 and 5 Å, see Figure 1a. Σ_2 has a double well and the second rise occurs at $\approx$ 40 fs when a fraction of the wave packet on Σ_2 reaches the second well region. Note that because their change is solely driven by the differences between the gradient on the PEC, the singular values computed for the dynamics without NAC vary more monotonically.

The discussion above suggests that up to 100 fs, the first three terms ($N_{min} = 3$ in Eq. (4)) in the singular decomposition, with a smaller role of the fourth one, should provide a good

approximation of the populations in electronic states and of the electronic coherences, which are elements of the partial electronic density, $\bar{\rho}_{el}(t)$ (Eq. (6)). As shown in Eq. (9), the elements of $\bar{\rho}_{el}(t)$ only depends on the electronic singular vectors $\mathbf{v}_n$. As can be seen from figure 7a, the electronic population in Σ_4 is essentially recovered with only the first two singular terms, since $\mathbf{v}_2$ is localized on Σ_4 (see figure 4c) when the wave packet is outside of the FC region, while for the population in Σ_2 (figure 7b), the third component is needed because $\mathbf{v}_3$ localizes on Σ_2 (figure 5a). Accordingly, electronic coherence Σ_2-Σ_4 (figure 8c) ~~are~~ is recovered with three terms as well. We show in the SI, figure S4, the plots for the populations in Σ_3 (Figure S4a) as well as the corresponding electronic coherences, Σ_3-Σ_4 and Σ_3-Σ_2, Figure S4b and c respectively. To recover the exact results for electronic populations and coherences that involve Σ_3, one needs to include the fourth component, as expected from figure 5c. Only the coherence Σ_3-Σ_4 is well approximated with $N_{min}=3$.
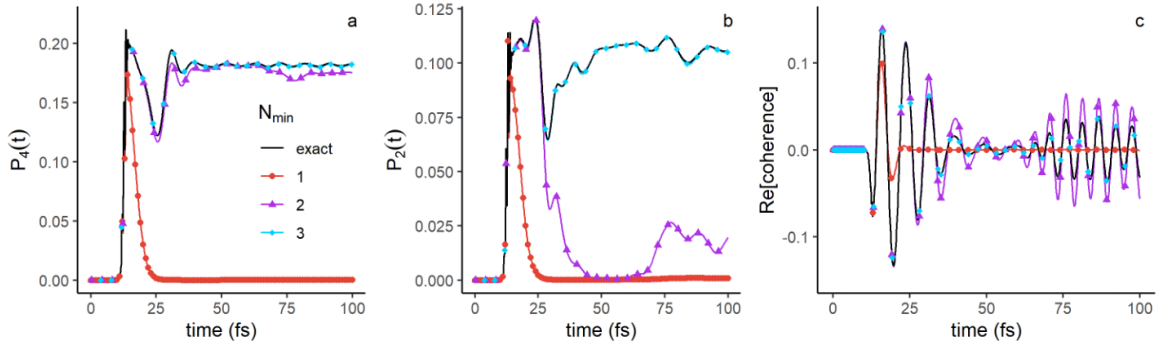

Figure 7. Approximation of the time evolution of the population of Σ_4 (a) and Σ_2 (b) and the electronic coherence Σ_2-Σ_4 (c) using an increasing number of singular values ($N_{min}=1$: red, $N_{min}=2$: violet and $N_{min}=3$: azure). The exact value is shown in full black lines.

We next discuss the approximation of three observables that depend on the full density matrix, $\rho(t)$, and cannot be cast into a trace on a partial density matrix, $\bar{\rho}_{el}$ or $\bar{\rho}_n$: the dipole moment, $\mu(t)$, the autocorrelation function, $|C(t)|^2$ and the nuclear momentum, $p(t)$ given respectively by

$$\mu(t) = Tr[\mu\rho(t)] = \sum_i \sum_{j,k} \mu_{jk}(g_i)\rho_{ij,ki}(t) \tag{15}$$

$$\left|C(t)\right|^2 = \mathrm{Tr}[\rho(0)\rho(t)] = \sum_{i,k} \sum_{jl} \rho_{ij,kl}(0)\rho_{ij,kl}(t) \tag{16}$$

$$p(t) = Tr[\hat{p}\rho(t)] = \sum_{ik} \sum_{jl} \rho_{ij,kl}(t)\left(p_{ik}\delta_{jl} + \tau_{jl}(g_i)\delta_{ik}\right) \tag{17}$$

The electric dipole moment, Eq. (15), is a crucial observable for all light-matter interactions. The autocorrelation function (Eq. ((16)) can be used to approximate the yield in high harmonics.[35] The nuclear momentum, Eq. (17), has both a nuclear dependence that can be written as a trace of the nuclear density matrix, $\overline{\rho}_n$, but it also possesses a contribution from the electronic motion and NAC. It is not an observable on a partial trace, but the contribution from the NAC term is small. The nuclear momentum might therefore be well approximated as an observable dependent on the nuclear density matrix only, neglecting the second term in the sum of Eq. (17).

Figure 8 shows that the three observables are well approximated by three singular values, ($N_{\min} = 3$ in Eq. (4)) with an even better description using four at longer times (not shown). The dipole moment (Figure 8a) depends on all the four populated electronic states, Σ_1, Σ_2, Σ_3 and Σ_4 and the electronic coherences between them. Since the autocorrelation function (Figure 8b) measures the overlap between the initial wave packet and the wave packet at a given time, the only significant contribution to this overlap is the contribution of the ground state in the FC region. As the part of the wave packet localized in the FC region requires only two singular values to be described, the autocorrelation function is fully described by the two largest singular values, and even by one singular value except shortly after the exciting pulse. The nuclear momentum (Figure 8c) essentially depends on the nuclear component of the singular terms, the $\mathbf{u}_n$ vectors. Two singular components are needed at short time, before 25fs, when the wave packets on the different electronic states are still in or in the vicinity of the FC regions. Three components are needed at longer times, to described the specific nuclear dynamics on each electronic state.
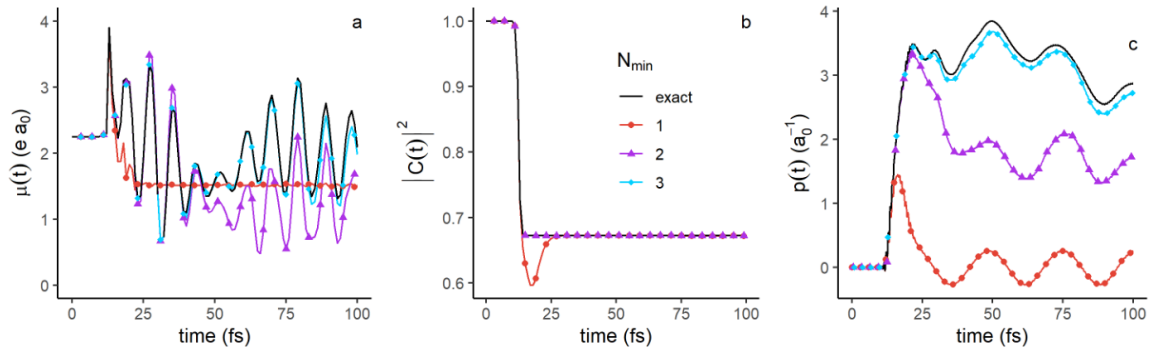
Figure 8. Approximation of the time evolution of the dipole moment (a), autocorrelation function (b) and nuclear momentum (c) with an increasing number, N_{min}, of singular values. The exact time evolution is given in full black lines. The legend is shown in the inset of panel b and is the same in as Figure 7.

4. Conclusions

We described a matrix representation which is suitable for the description of the wave function of entangled systems. The decomposition of the matrix by its singular values and vectors is equivalent to the Schmidt decomposition of the system and provides us with a measure of the entanglement. The physical meaning of the singular vectors was discussed, as well as their direct connection with partial density matrices. We also described how an approximation of the partial density matrices and of the observables depending on the full density matrix can be computed from the SVD. The theoretical framework was then applied to the study of the photoexcitation of the LiH molecule, in which we illustrated the physical meaning of singular vectors in the molecular system and showed that only a few singular values were required in order to approximate well the dynamics. Furthermore, the origin of changes in time in the entanglement of the molecule is shown to be due to the motion of wave packets of different electronic states on the grid. Two effects were observed as the causes of this motion: the leading effect was the interaction with the exciting optical pulse, but an additional nuclear motion was caused by the NACs. Finally, we showed numerically that partial density matrices elements and related observables could be well approximated using few terms of the singular decomposition.

Conflicts of interest

There are no conflicts to declare.

Acknowledgements

Footnote

† Supplemental figures S1, S2, S3, S4 and S5 are available in the Electronic supplementary information (ESI).

References

(1). U. Graf, M. Fieß, M. Schultze, R. Kienberger, F. Krausz and E. Goulielmakis, *Opt. Express*, 2008, **16**, 18956-18963.

(2). M. Galli, V. Wanie, D. P. Lopes, E. P. Månsson, A. Trabattoni, L. Colaizzi, K. Saraswathula, A. Cartella, F. Frassetto, L. Poletto, F. Légaré, S. Stagira, M. Nisoli, R. Martínez Vázquez, R. Osellame and F. Calegari, *Opt. Lett.*, 2019, **44**, 1308-1311.

(3). L. Bruder, L. Wittenbecher, P. V. Kolesnichenko and D. Zigmantas, *Opt. Express*, 2021, **29**, 25593-25604.

(4). B. A. Horn, J. L. Herek and A. H. Zewail, *J. Am. Chem. Soc.*, 1996, **118**, 8755-8756.

(5). T. Latka, V. Shirvanyan, M. Ossiander, O. Razskazovskaya, A. Guggenmos, M. Jobst, M. Fieß, S. Holzner, A. Sommer, M. Schultze, C. Jakubeit, J. Riemensberger, B. Bernhardt, W. Helml, F. Gatti, B. Lasorne, D. Lauvergnat, P. Decleva, G. J. Halász, Á. Vibók and R. Kienberger, *Phys. Rev. A*, 2019, **99**, 063405.

(6). A. Picchiotti, A. Nenov, A. Giussani, V. I. Prokhorenko, R. J. D. Miller, S. Mukamel and M. Garavelli, *J. Phys. Chem. Lett.*, 2019, **10**, 3481-3487.

(7). R. Borrego-Varillas, A. Nenov, L. Ganzer, A. Oriana, C. Manzoni, A. Tolomelli, I. Rivalta, S. Mukamel, M. Garavelli and G. Cerullo, *Chem. Sci.*, 2019, **10**, 9907-9921.

(8). T. Kobayashi and Y. Kida, *Phys. Chem. Chem. Phys.*, 2012, **14**, 6200-6210.

(9). B. A. West, B. P. Molesky, P. G. Giokas and A. M. Moran, *Chem. Phys.*, 2013, **423**, 92-104.

(10). E. Baldini, T. Palmieri, E. Pomarico, G. Auböck and M. Chergui, *ACS Photonics*, 2018, **5**, 1241-1249.

(11). S. A. Jayantha, K. G. Komarova, S. v. d. Wildenberg, F. Remacle and R. D. Levine, in *Attosecond Molecular Dynamics*, eds. M. J. J. Vrakking and F. Lepine, Royal Society of Chemistry, Cambridge, 2018, vol. 13, pp. 308-347.

(12). A. Valentini, S. van den Wildenberg and F. Remacle, *Phys. Chem. Chem. Phys.*, 2020, **22**, 22302-22313.

(13). A. Ekert and P. L. Knight, *Am. J. Phys.*, 1995, **63**, 415-423.

(14). M. A. Nielsen and C. I. L., *Quantum Computation and Quantum Information*, Cambridge University Press, Cambridge, 2010.

(15). R. Horodecki, P. Horodecki, M. Horodecki and K. Horodecki, *Rev. Mod. Phys.*, 2009, **81**, 865-942.

(16). A. Aspect, J. Dalibard and G. Roger, *Phys. Rev. Lett.*, 1982, **49**, 1804-1807.

(17). A. Aspect, P. Grangier and G. Roger, *Phys. Rev. Lett.*, 1982, **49**, 91-94.

(18). X.-W. Hou, J.-H. Chen and Z.-Q. Ma, *Phys. Rev. A*, 2006, **74**, 062513.

(19). J. Li and S. Kais, *Sci. Adv.*, 2019, **5**, eaax5283.

(20). J. Li, M. Sajjan, S. S. Kale and S. Kais, *Adv. Quantum Technol.*, 2021, 2100098.

(21). J. L. Sanz-Vicario, J. F. Pérez-Torres and G. Moreno-Polo, *Phys. Rev. A*, 2017, **96**, 022503.

(22). L. K. McKemmish, R. H. McKenzie, N. S. Hush and J. R. Reimers, *J. Chem. Phys.*, 2011, **135**, 244110.

(23). D. J. Haxton, K. V. Lawler and C. W. McCurdy, *Phys. Rev. A*, 2011, **83**, 063416.

(24). D. J. Haxton, K. V. Lawler and C. W. McCurdy, *Phys. Rev. A*, 2015, **91**, 062502.

(25). M. Vatasescu, *Phys. Rev. A*, 2013, **88**, 063415.

(26). A. F. Izmaylov and I. Franco, *J. Chem. Theory Comput.*, 2017, **13**, 20-28.

(27). M. Nisoli, P. Decleva, F. Calegari, A. Palacios and F. Martín, *Chem. Rev.*, 2017, **117**, 10760-10825.

(28). M. J. J. Vrakking and F. Lepine, eds., *Attosecond molecular dynamics*, The Royal Society of Chemistry, Cambridge, 2019.

(29). I. C. D. Merritt, D. Jacquemin and M. Vacher, *J. Phys. Chem. Lett.*, 2021, **12**, 8404-8415.

(30). M. J. J. Vrakking, *Phys. Rev. Lett.*, 2021, **126**, 113203.

(31). T.-D. Bradley, E. M. Stoudenmire and J. Terilla, *Machine Learning: Science and Technology*, 2020, **1**, 035008.

(32). wikipedia, wikimedia foundation, https://en.wikipedia.org/wiki/Vectorization_(mathematics), 2021.

(33). G. H. Golub and C. Reinsch, in *Linear Algebra*, eds. J. H. Wilkinson, C. Reinsch and F. L. Bauer, Springer Berlin Heidelberg, Berlin, Heidelberg, 1971, pp. 134-151.

(34). S. van den Wildenberg, B. Mignolet, R. D. Levine and F. Remacle, *J. Chem. Phys.*, 2019, **151**, 134310.

(35). M. Lein, *Phys. Rev. Lett.*, 2005, **94**, 053004.